Improved axial plane distance and velocity determination for ultrafast electron beam X-ray computed tomography

Neumann, M.; Bieberle, M.; Wagner, M.; Bieberle, A.; Hampel, U.;

Improved axial plane distance and velocity determination for ultrafast electron beam X-ray computed tomography

Martin Neumann[1], Martina Bieberle[2], Michael Wagner[1], André Bieberle[2], Uwe Hampel[1,2]

[1] Chair of Imaging Techniques in Energy and Process Engineering,

Technische Universität Dresden, 01062 Dresden, Germany.

[2] Helmholtz-Zentrum Dresden - Rossendorf, Institute of Fluid Dynamics,

Bautzner Landstr. 400, 01328 Dresden, Germany.

Email: martin.neumann@tu-dresden.de

Abstract

Ultrafast electron beam X-ray computed tomography (UFXCT) has in recent years become an indispensable tool for multiphase flow studies. An essential feature of this technique is fast cross-sectional imaging in two distinct planes. Both the spatial location of focal spot path and detectors as well as the angular scanning range in UFXCT differ from that of conventional X-ray CT systems. This brings in a spatial dependence in axial scanning position and resolution. In this paper, we present an analysis of this problem, which results in an improved description of the location and shape of the imaging regions, a more accurate map of the distance between the imaging planes and finally a higher precision in the determination of axial structure velocities. The benefit of this improved approach is exemplarily demonstrated for a two-phase pipe flow around an obstacle.

Key words: ultrafast X-ray computed tomography, phase velocity measurement

1. Introduction

Ultrafast electron beam X-ray computed tomography (UFXCT) [1][2] is a novel fast imaging technique for non-invasive investigations of multiphase flows. It has for example been used to study gas-liquid two-phase flows in pipes [3], slurry bubble columns [4] and ceramic foams [5], as well as gas-solid two-phase flow in conventional [6] and spout fluidized beds [7]. UFXCT provides cross-sectional images of the phase distribution in a flow with high speed (up to 8000 frames per second) and high spatial resolution (~ 1 mm). The UFXCT scanner consists of an electron beam gun, a horseshoe shaped tungsten target for X-ray generation and a static dual plane detector ring (Figure 1).

The electron gun produces a free electron beam with a maximum energy of 150 keV. The electron beam is focused and guided on the tungsten target using focusing and deflection coils, and thus, generates a moving X-ray source spot that rotates around the object of investigation. With this scheme, very high deflection frequencies f and thus imaging rates can be achieved. The X-ray radiation is attenuated while passing the object of investigation. Its intensity is measured by a fast multichannel detector that is synchronized with the beam deflection. Thus, a set of projection data is obtained that includes the attenuation values of all X-ray paths (or rays) from various angular focal spot positions to all detector elements behind the object. The projection data set from each beam revolution can then be used to reconstruct a non-superimposed cross-sectional image using CT reconstruction algorithms like the filtered back projection algorithm [8].
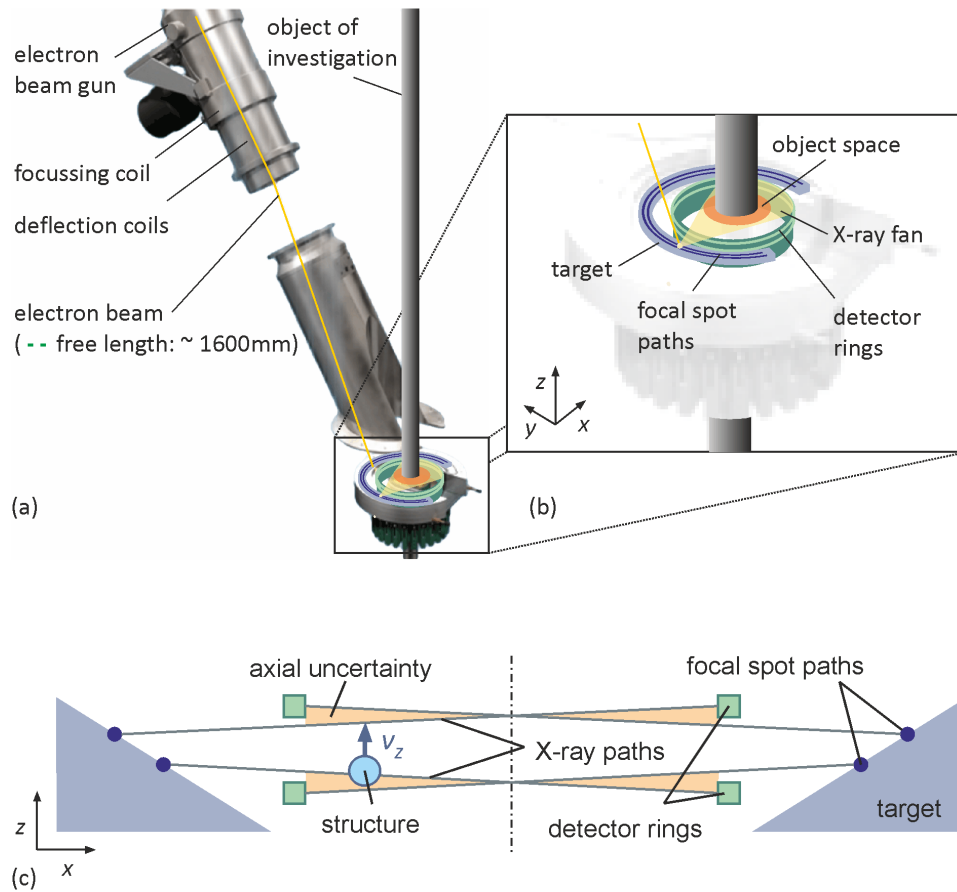
Figure 1: *Basic principle of UFXCT (a) with schematic close up of measurement area for dual plane CT mode (b) and illustration of the axial uncertainty problem (c) (not to scale). As the focal spot path and the detector ring are not axially co-aligned, structures contribute to the X-ray attenuation in different axial locations.*

The UFXCT scanner performs scanning in two planes, which is mainly intended for determining the axial velocities of structures passing the planes via a time-of-flight method [9]. For this dual plane CT mode, the electron beam is guided alternatingly along two axially displaced focal spot paths on the tungsten target and the data of the respectively associated ring of detector elements is evaluated. It consequently results in two time series of cross-sectional images of the same process with alternating time stamps as can be seen in Figure 2.
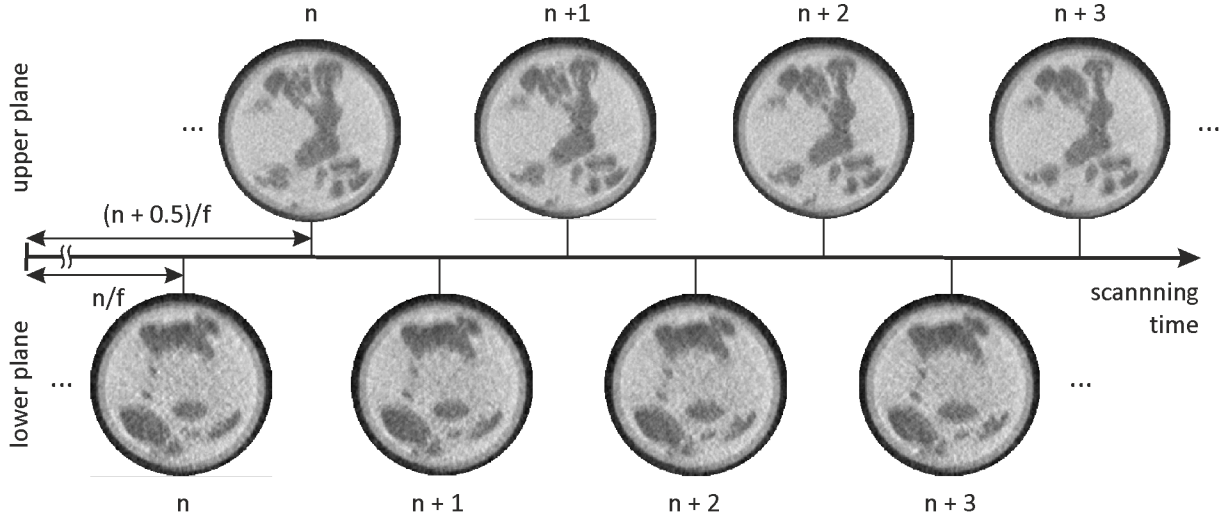
Figure 2: Scanning regime of dual plane CT scaning mode with alternatingly recorded cross-sectional images for both measurement planes.

For a precise determination of the structure's velocity, an unambiguous knowledge of the distance between the two measurement planes is mandatory. In recent studies, both measurement planes were assumed to be parallel and thus have a constant distance across the entire imaged cross-section. The distance value itself was mainly specified by consideration of the scanner design and the steering parameters of the electron beam. As will be shown below, this simplified assumption is not too bad when looking at a cross-section averaged velocity. However, the effective image plane distance has got a significant spatial dependence and hence local axial velocity calculation should account for that.

The axial velocity v_z of the structure can be quantified by

$$v_z = \Delta z \cdot \Delta t^{-1}, \tag{1}$$

wherein Δt is the time interval the structure needs to cover the axial distance Δz between both measurement planes at its respective (x, y)-position. There are different approaches for determining Δt from time series data, such as cross-correlation or single particle tracking. Their characteristics, advantages, disadvantages and accuracies are discussed elsewhere [5]. The focus of this work lies on the characterization of the distance Δz, which is given by the axial positions of the two planes. In case of UFXCT, for several reasons those positions are not that well defined. First of all, the principle

of UFXCT requires a small axial offset between a focal spot path and its corresponding detector ring (Figure 1c). Therefore, each point of a tomographic image is synthesized from the attenuation of a few hundred rays that do not intersect at a single axial position. The resulting axial intersection position distribution is furthermore non-symmetric as there is a limited angular scanning range due to the horseshoe shaped target. Hence, not only the spread of the ray intersections but also the mean intersection position is spatially dependent. Thus, the imaging plane is actually not a real plane, but a spatially expanded imaging region, which is not symmetric. Finally, uncertainties in the electron beam steering lead to more uncertainties of the final focal spot path positions. The next section describes how the plane distance can still be assessed.

2. Methods for the plane distance evaluation

2.1. Theoretical approach for the evaluation of the axial plane distance

The arrangement of the detector elements on the two detector rings is known and for the position of the two focal spot paths of the X-ray source predictions according to the beam deflection parameters do exist. However, deriving the z-position distributions of each imaging plane and subsequently the plane distance $\Delta z(x, y)$ from such geometrical information is not straightforward. As has been described above, the multiple rays between focal spot positions and detector elements do propagate and intersect neither within one plane nor within a curved surface. Instead, the rays are spread in a certain region around a surface, which is asymmetrically bent due to the opening in the target. During reconstruction, the projection lines from each of the two imaging planes are treated as being originating from within one 2D plane. This assumption is sufficient for imaging as the axial deviations are small and can thus be treated as slight axial integration. However, for velocity determination, a more accurate position information would be valuable and can be achieved by taking the three-dimensionality of the X-ray propagation into account.

The evaluation of the plane distance has been performed based on the geometrical conditions given in Figure 3. Therein, an imaging region of diameter 140 mm is considered. In order to retrieve the

distribution of the axial positions within the tomographic images, the following strategy mimicking the CT data acquisition and reconstruction is proposed. In a first step, the object space is discretized into voxels of equal edge length of 1 mm over a height of 12 mm. A three-dimensional ray-to-voxel mapping is then calculated according to the defined geometrical parameters using the nearest neighbor approach [10]. Using this mapping, a forward projection of a homogeneous object distribution along the given projection lines is performed followed by a back projection of the resulting projection values onto a new blank distribution defined on the same voxel grid.
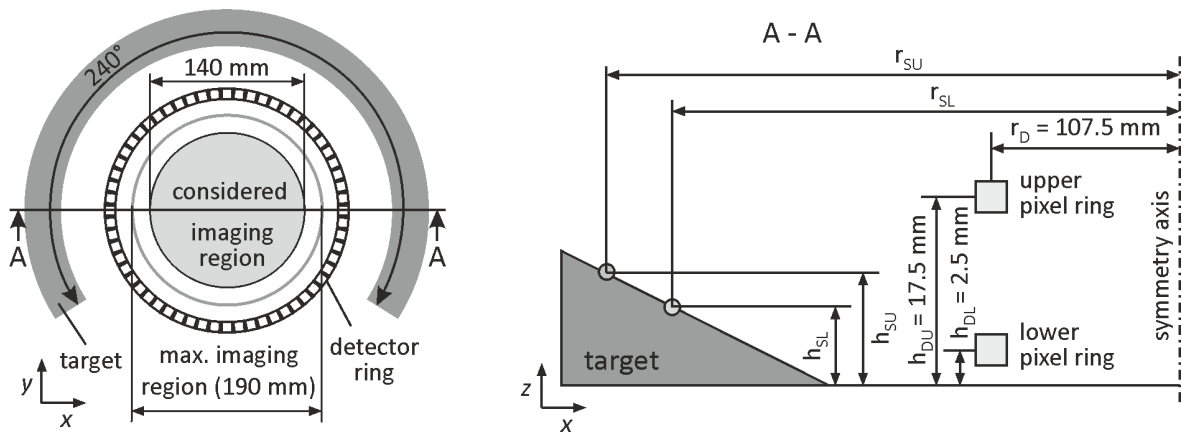

Figure 3: Schematic top and sectional view of the UFXCT scanner head with indicated imaging region and geometrical parameters considered in the theoretical approach.

The resulting three-dimensional distribution (Figure 4) thus represents the weighted spatial domain, from which a 2D reconstructed image is acquired by the described imaging modality. The actual axial positions of this imaging region are derived by calculating the balance point in axial direction for each point (x, y) in the image domain. Finally, the difference between the axial positions of the upper and the lower plane yields the plane distance distribution. As the focal spot path spans only 240°, the resulting plane distance is not equally distributed (Figure 4).
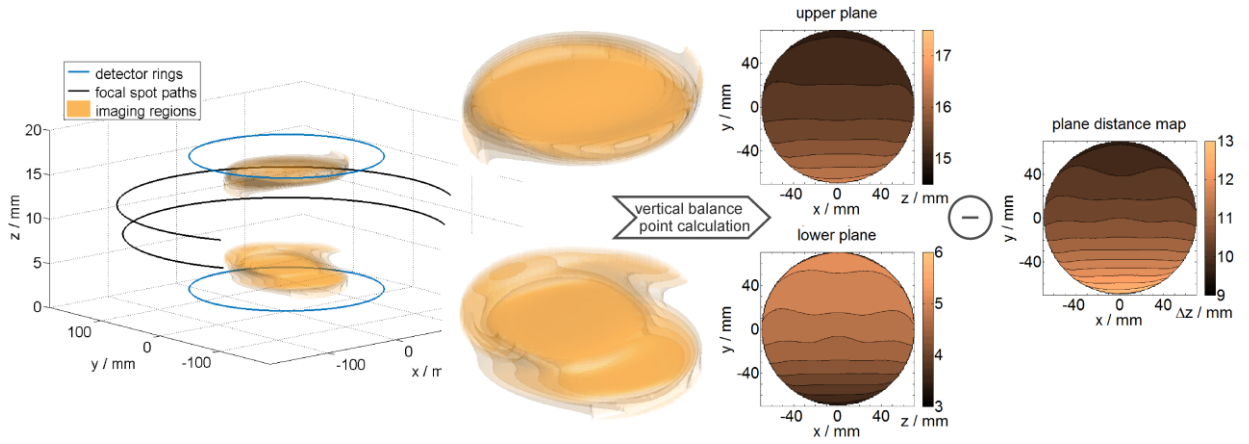
Figure 4: Illustration of simulated imaging regions (as multiple contour plot) within the geometry of the UFXCT and derivation of axial position maps and the plane distance map.

The parameters of the focal spot paths have been varied to study the sensitivity of the axial plane distance distribution on deviations of the geometrical conditions.

Table 1 lists the analyzed parameters for the lower as well as the upper source spot path in terms of radius (r_S) and height (h_S) (index l and u respectively). In total, this gives 16 combinations of upper and lower source spot paths, covering a certain range around the chosen parameters of the electron beam steering. Furthermore, the influence of the focal spot size s on the resulting imaging region has been investigated, as the true spot size depends on the beam current and other steering parameters and is also subject to small deviations during long measurement campaigns. In [11] the focal spot size has been measured as a function of the beam current, which revealed values in the range 0.7 mm $\leq s \leq$ 1.6 mm. Therefore, a range of 0.5 mm $\leq s \leq$ 2.0 mm has been considered in this analysis.

Table 1:   Geometric parameters for the calculation of axial position maps for lower (L1-L4) and upper (U1-U4) CT measurement planes.

	L1	L2	L3	L4		U1	U2	U3	U4
r_{SL} / mm	183.5	182.5	181.5	180.5	r_{SU} / mm	184.0	185.0	186.0	187.0
h_{SL} / mm	10.2	9.7	9.2	8.7	h_{SU} / mm	10.5	11.0	11.5	12.0

2.2. Experimental determination of the axial plane distance

In order to validate the theoretically derived plane distance maps, an experimental study based on structures with known velocities has been conducted. At the same time, the assumptions on the parameters of the focal spot paths can be verified.

2.2.1. Setup and measurement procedure

For the experimental determination of the axial distance between the two UFXCT scanning planes a setup is proposed that provides uniformly moving objects with known velocity to derive the plane distance from the temporal shift between the image sequences of both planes. For this purpose, a tooth belt with a geometry of the teeth as indicated in Figure 5a is used. As the teeth form a large number of objects with uniform speed, a better accuracy compared to a single object is achieved. The tooth belt is installed as shown in Figure 5b and is driven by a step-less controllable servo motor.
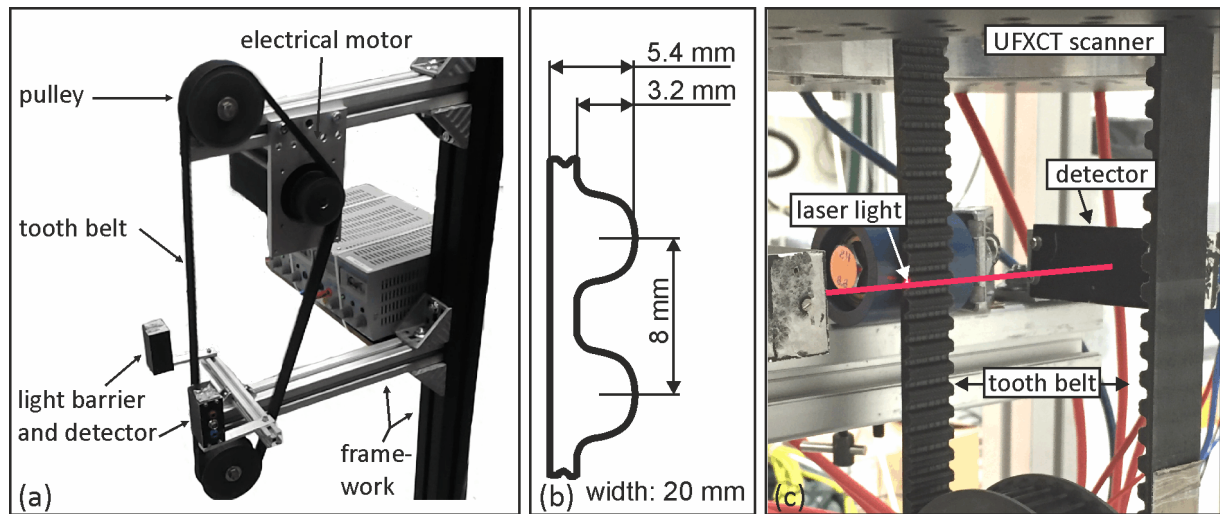

Figure 5: *Illustration of the tooth belt setup for experimental determination of axial distance between the UFXCT scanning planes (a), geometry of the teeth (b), Close-up of the light barrier sensor alignment for the measurement of the tooth belt velocity.*

Due to the behavior of the motor control unit and friction losses of the tooth belt, the circumferential velocity is not exactly known in advance and may even vary slightly during operation. Therefore, the experimental setup additionally comprises a light barrier sensor with a focal spot of about 1.5 mm and a switching time of 20 ns to provide a highly accurate and time resolved position

signal, from which the actual velocity of the belt can be derived. It is installed such that the laser beam is directed along the belt at the position of the teeth as shown in Figure 5c. The analog output signal of the photo detector is simultaneously sampled by the UFXCT electronics as external signal with the same sampling rate (1 MHz) as the X-ray detectors.
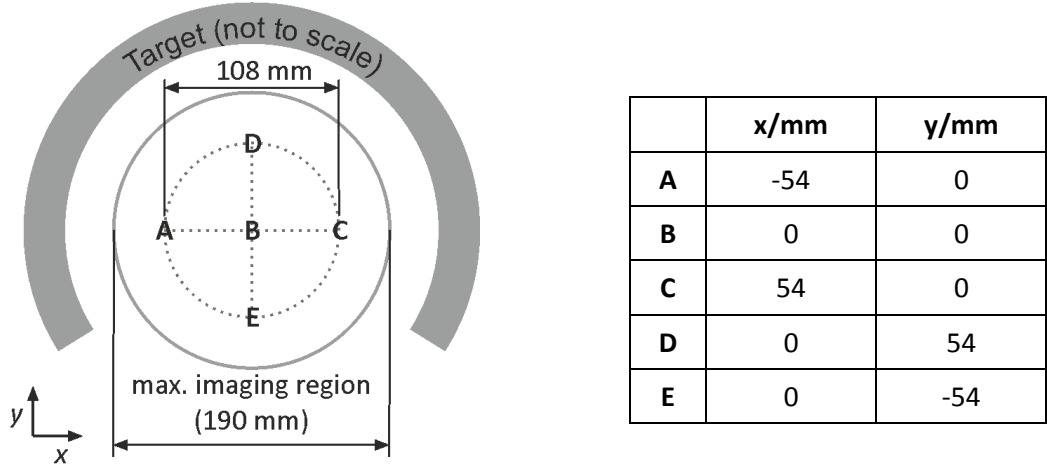

	x/mm	y/mm
A	-54	0
B	0	0
C	54	0
D	0	54
E	0	-54

Figure 6: Schematic top view of the the UFXCT scanner with indicated tooth belt measurement positions within the cross-section.

The tooth belt has been positioned at five different locations within the imaging region of the UFXCT scanner as indicated in Figure 6. The deflection frequency of the UFXCT was set to $f = 4\,\text{kHz}$ resulting in of 2,000 fps per plane as one of the most common frame rates of UFXCT for multiphase flow experiments. The velocity of the tooth belt was chosen in a way to reach an axial spatial resolution between 0.1 mm and 0.2 mm, which lead to a value of 0.27 m/s. Data was recorded for 10 s resulting in two image sequences of $N = 20.000$ frames each.

2.2.2. Data processing

To extract 1D time series out of the reconstructed image sequences, averaging within a confined window around the tooth belt (Figure 7a) is performed in every frame. Thus, periodical time series of the averaged attenuation coefficient $\bar{\mu}_L(n)$, $\bar{\mu}_U(n)$ corresponding to the cross-sectional area of the tooth belt in the lower and upper plane, respectively, are obtained. The frame index n represents the

measurement time $t = (n + \Delta n)/f$ with Δn being 0 and 0.5 for the lower and upper plane, respectively.
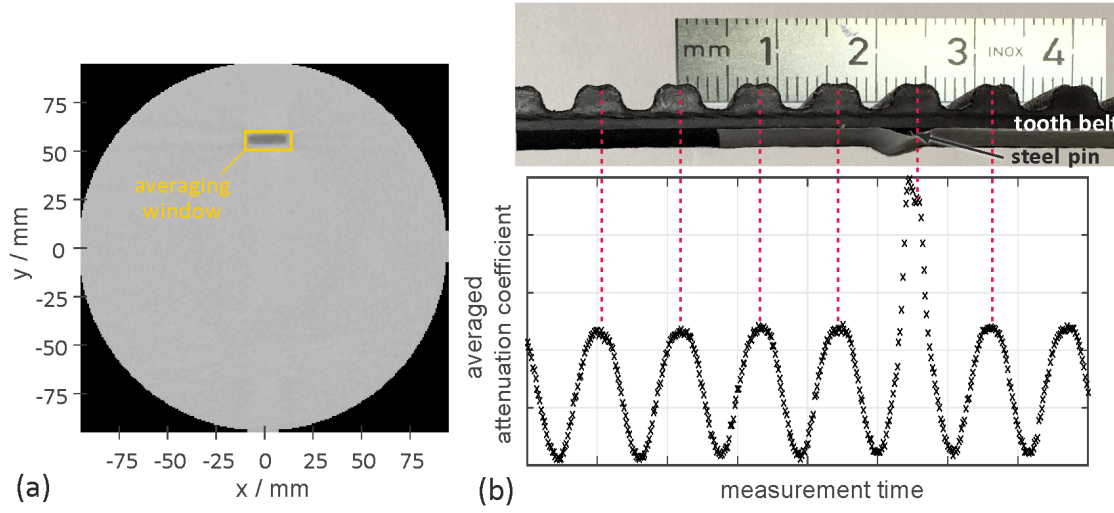

Figure 7: *Reconstructed image of the tooth belt at position D with visualized averaging window (a) and tooth belt section with corresponding series of the averaged attenuation coefficient $\overline{\mu}_U(n)$ within the averaging window (b).*

To deduce a time shift between the two signals $\overline{\mu}_L(n)$ and $\overline{\mu}_U(n)$, the same structures have to be identified in both signals. As the tooth belt provides a repetitive structure, the explicit assignment of the attenuation signal of a specific tooth in both planes is not given apparently. From geometrical considerations, it is assumed to find a certain tooth peak in the next but one tooth peak in the second signal, as the distance between two teeth is 8 mm and the plane distance is expected at a noticeably higher value. Nevertheless, to clearly identify the teeth in both planes, a steel pin was mounted at one position of the tooth belt as an indicator of the resulting time shift. Thus, the considerably higher peak in the averaged attenuation coefficient signal represents the passing of the marked tooth, as can be seen in Figure 7b.

To quantify the time shift between both averaged attenuation coefficient series, the cross correlation function

$$C(k) = \begin{cases} \frac{1}{N-k}\sum_{n=0}^{N-1-k}\overline{\mu}_U(n) \cdot \overline{\mu}_L(n+k) & \text{for } k \geq 0 \\ \frac{1}{N-k}\sum_{n=|k|}^{N-1}\overline{\mu}_U(n) \cdot \overline{\mu}_L(n+k) & \text{for } k < 0 \end{cases},$$ (2)

has been calculated. As can be seen in Figure 8, in accordance with the assumption, the time shift between the steel pin peaks corresponds to the second maximum of the cross correlation function in the direction of positive (negative) shift values k for downward (upward) movement of the belt. Therefore, the position k_{xc} of the second positive (or negative) peak of $C(k)$ is deduced for any further evaluation of the time shift.
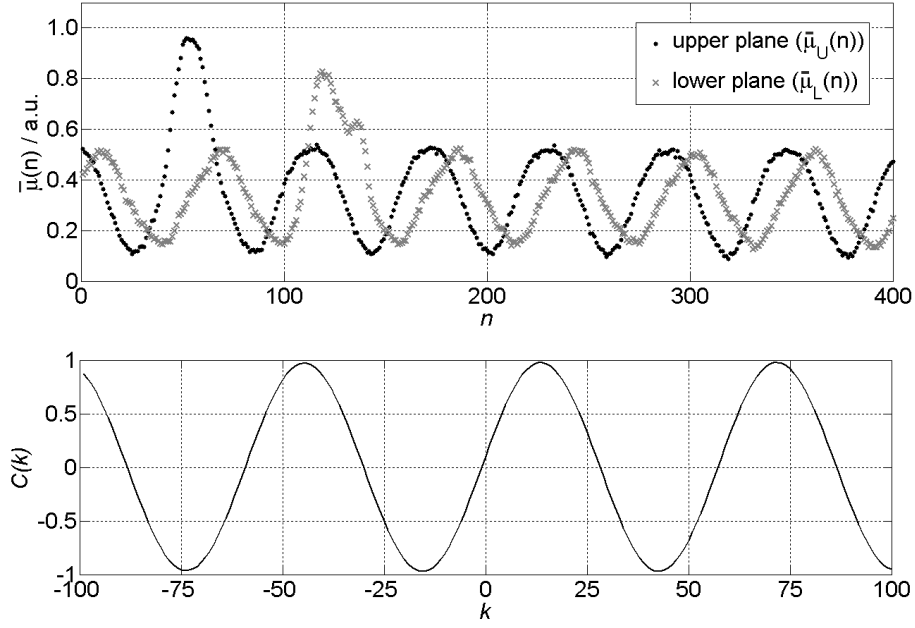

Figure 8:   Averaged attenuation coefficient series from both planes and corresponding cross correlation function.

Beside the global time shift deduced from the global cross correlation function $C(k)$ calculated from Eq. 2, a temporally resolved time shift can be derived by applying the cross correlation only to parts of the averaged attenuation coefficient signal using a window of size N_W yielding

$$C_n(k) = \frac{1}{N_W} \sum_{i=1}^{N_W} \overline{\mu}_L(n+i) \cdot \overline{\mu}_U(n+i+k) \,. \tag{3}$$

The resulting $k_{\mathrm{xc}}(n)$, which have been derived in the same way as k_{xc}, are determined within a range of $k_{\max} \leq n \leq N - k_{\max}$. As the expected time shift is fairly below 100 frames, a maximal shift value $k_{\max} = 100$ and a window size of $N_W = 100$ have been chosen. Other values showed to have little effect on the final results.

The light barrier provides a continuous binary signal, where the high state represents the time of an undisturbed (gap) and the low state a blocked (tooth) laser-detector path. Since the light barrier is simultaneously sampled with 1 MHz, the exact movement time of the active tooth belt section can be extracted from the measured signal with high precision. The movement time of one tooth at a time is taken into account, in order to calculate the current velocity from the measured time intervals. Thus, the reference velocity is calculated as $v_{\text{ref}}(n) = d/\Delta t_{LB}(n)$, where $d = 8$ mm is the distance between two teeth and $\Delta t_{LB}(n)$ is the time interval between the passage of two adjacent teeth determined from slopes in the light barrier signal in the vicinity of n. Because of its enclosed structure, the tooth belt provides a nearly constant velocity across the entire length, which is only affected by temporal deviations of the electrical motor. This allows a direct comparison of the measured reference velocity with the cross-correlated velocity information of the tomographic measurements.

Finally, the determined frame shifts $k_{\text{xc}}(n)$ from the UFXCT measurements and the reference velocity $v_{\text{ref}}(n)$ from the light barrier signal are used to calculate the plane distance following Eq. 1 as

$$\Delta z(n) = v_{ref}(n) \frac{|k_{\text{xc}}(n) - 0.5|}{f}. \tag{4}$$

3. Results

3.1. Derivation of axial plane distance maps by theoretical analysis

By applying the presented theoretical analysis, axial height maps of the lower and upper measurement planes have successfully been determined and plane distance maps have been derived accordingly. All combinations of the parameters given above including different focal spot sizes have been analyzed.

Figure 9 shows the resulting plane distance maps for all considered focal spot paths with a focal spot size of 1 mm. As can be seen, the distance maps are similarly shaped for all the considered cases.

They are symmetric along the (vertical) symmetry line of the underlying geometry, as expected, and the plane distance increases towards the opening of the target, i.e for smaller y. At constant y-positions, the plane distance increases slightly from the center towards the edge. The main difference between the maps is the mean value $\overline{\Delta z}$ of the plane distance (Figure 10), which depends on the positions and distances of the focal spot paths. This mean value is nearly proportional to the axial focal spot path distance with $\overline{\Delta z} \approx 0.3(h_{SU} - h_{SL})$.
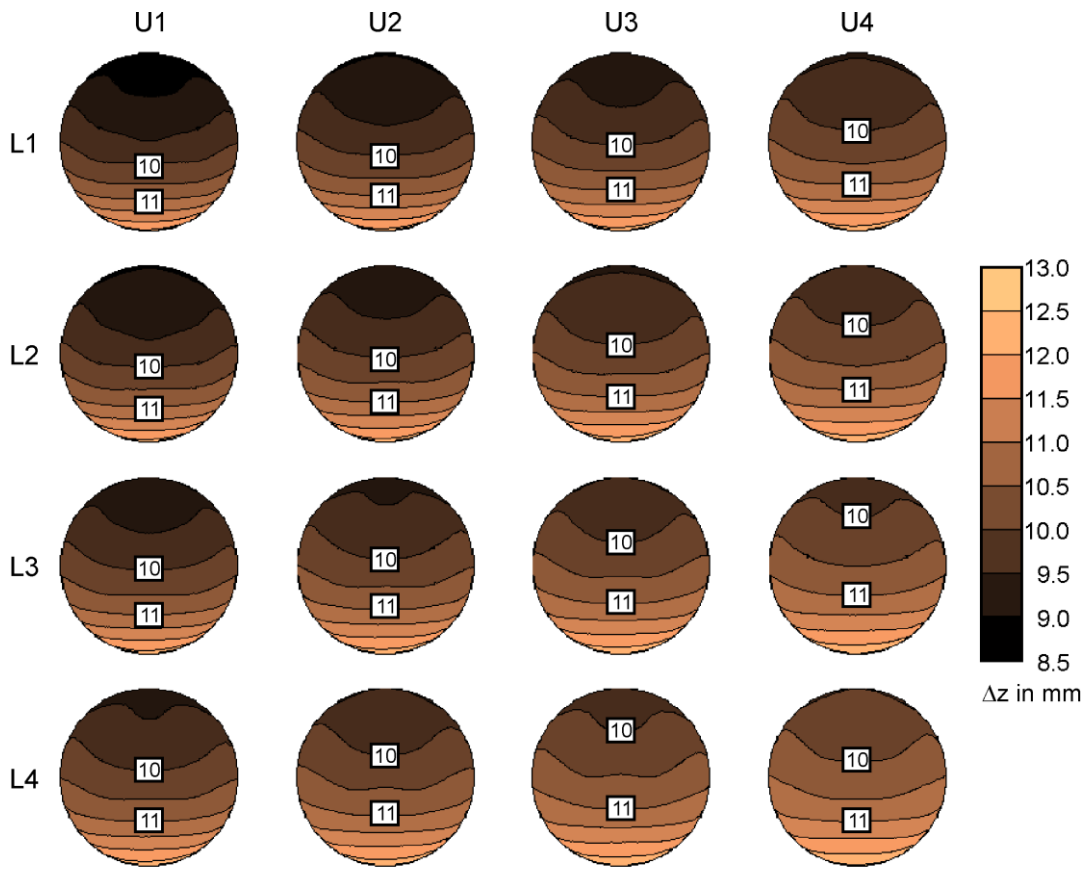

Figure 9: Determined plane distance maps for all considered focal spot paths (according to Table 1) and a focal spot size of 1 mm.
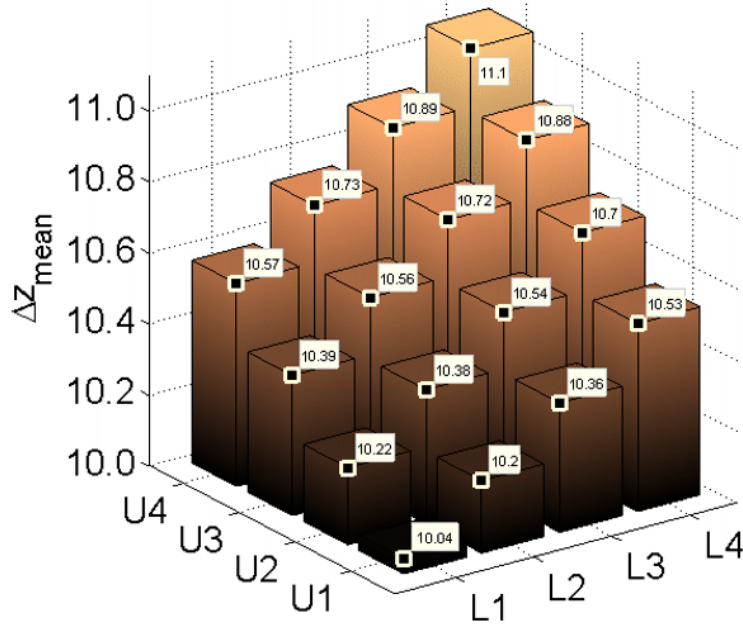
Figure 10: Mean plane distances for all considered focal spot paths (according to Table 1) and a focal spot size of 1 mm.

The influence of the focal spot size on the resulting plane distance map is shown in Figure 11. As can be seen, the shape changes significantly with the focal spot size, which can be explained by the different width of the beams near the target in comparison to their width near the detector. The part of the plane distance map, which is close to the opening of the target, is only little affected, because the geometry in this region is dominated by the detector. The x- and y-profiles in Figure 11 illustrate the character of the shape differences: while the central line at $x = 0$ is comparable for all focal spot sizes, the shape at constant y is quite different.
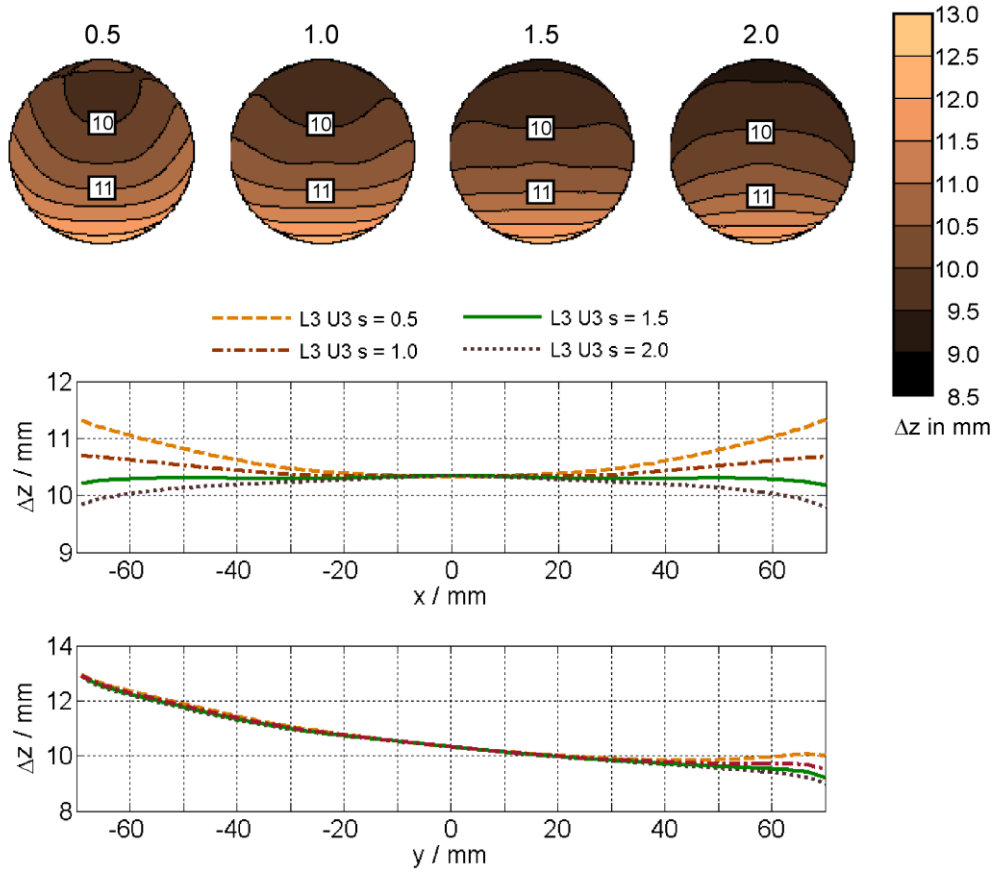
Figure 11: Determined plane distance maps and central profiles for different focal spot sizes for the focal spot path L3-U3.

3.2. Experimentally determined plane distances

The axial plane distance is experimentally investigated by applying the described signal processing steps yielding the temporally resolved plane distance $\Delta z(n)$. In Figure 12 this signal is exemplarily shown for the positions B, D and E. The plane distance slightly deviates over measurement time, but shows no recognizable drifting behavior. It is assumed that these deviations are caused by slightly varied focal spot paths for every revolution of the electron beam due to inevitable effects of the deflection system.
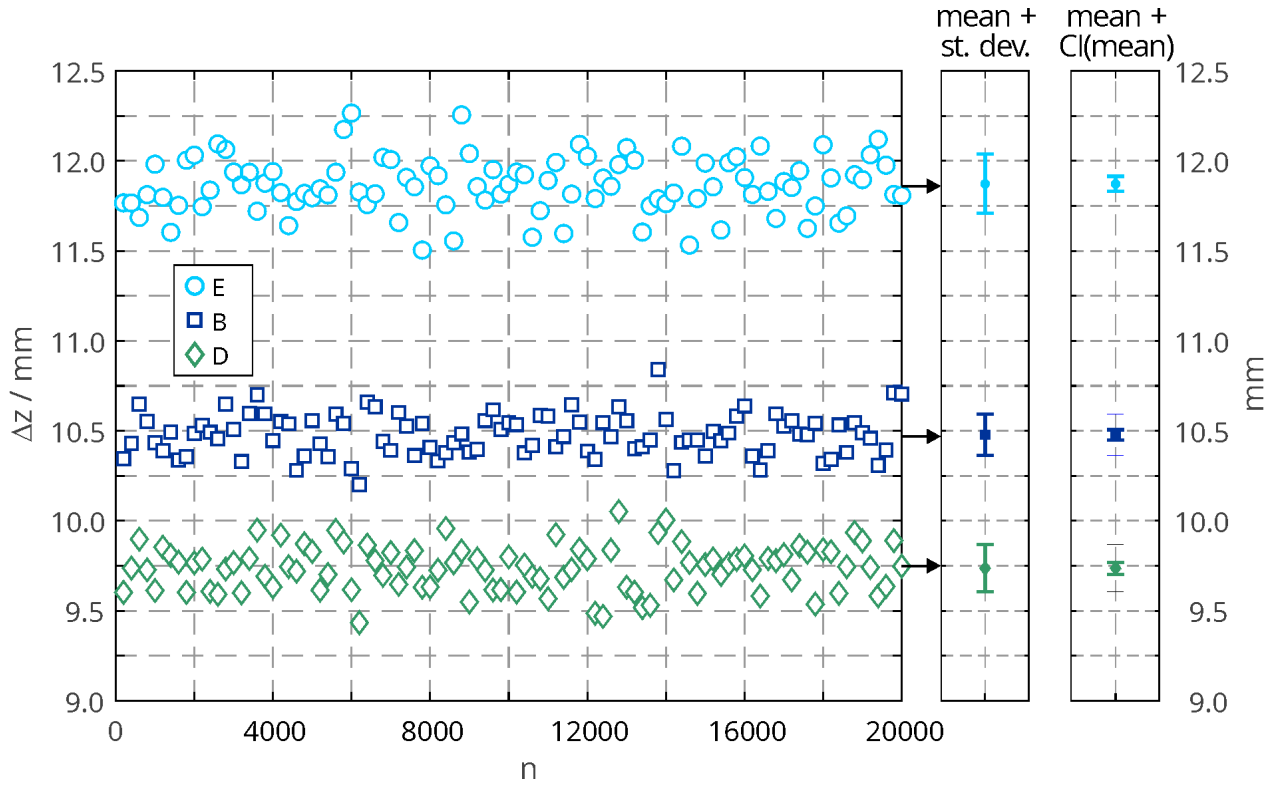
Figure 12: Resulting axial plane distance $\Delta z(n)$ at three exemplary positions (left) and derived mean value, standard deviation and confidence intervall (right).

Since the deviations of the axial plane distance determined in this experiment seem to be stochastic, a mean distance value $\overline{\Delta z}$ and its standard deviation s are calculated for every measurement position, as is illustrated on the right side of Figure 12. The standard deviation is in all cases below 0.2 mm, which corresponds to an uncertainty of about ± 2 % for one measurement value. Extended to the estimation of the mean of 100 values, a confidence interval of $\left[\overline{\Delta z} \pm \frac{s}{\sqrt{100}} p\right]$, with p being the quantile of the normal distribution for the desired confidence level, can be determined. For example, a confidence level of 99 % would give $\left[\overline{\Delta z} \pm 0.05 \text{ mm}\right]$.

3.3. Comparison of measured and calculated plane distances

The various simulated plane distance distributions have been compared with the resulting distances from the measurements at the five positions defined above. The best agreement could be achieved with the L3-U3 and the L3-U4 configuration at spot sizes of $s = 1.0$ mm and $s = 1.5$ mm as shown in Figure 13. Based on these results, another configuration with the same lower focal spot path position

(L3) and an upper focal spot path between U3 and U4 ($r_{Su} = 186.5$ mm) as well as a source spot size of $s = 1.2$ mm has been evaluated to further improve the agreement between the experimental results and the calculated plane distance map. The resulting profiles as well as the whole plane distance map of this optimized configuration are depicted in Figure 13.
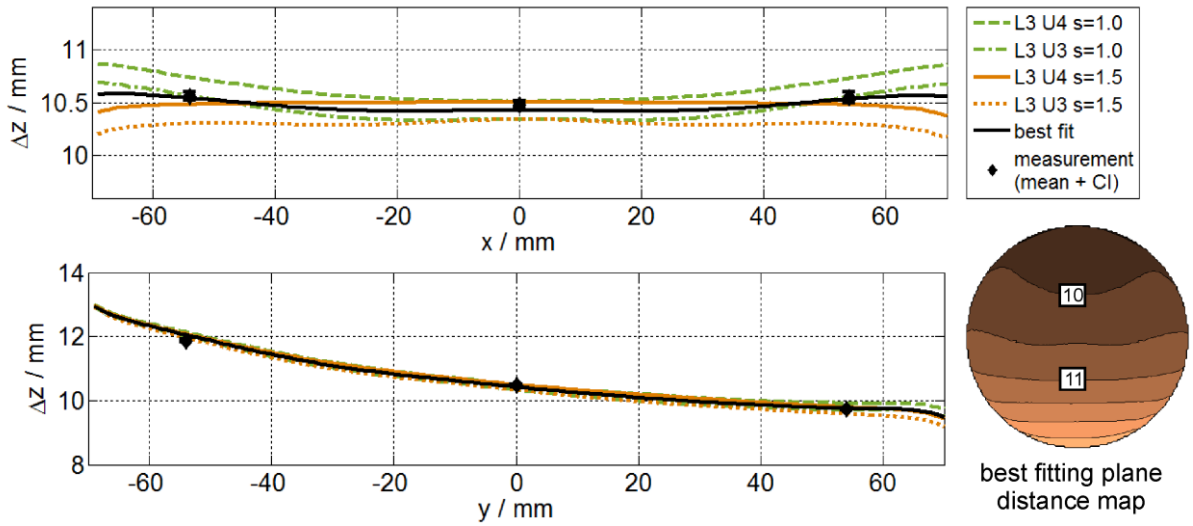

Figure 13: Comparison of the experimentally determined plane distance at five measurement positions and the theroretically determined distributions with the best match. Beside the four closest distributions from the simulation study, one additional result from an optimized configuration ($r_{SL} = 181.5\ mm, r_{SU} = 186.5\ mm, s = 1.2$ mm) is plotted.

This final plane distance map, which has been approved by the tooth belt measurements, can now be used to calculate axial velocity maps from two-plane ultrafast X-ray computed tomography.

3.4. Application to two-phase pipe flow

As an example for practical application of the described method, velocity distributions of an upward water-air two-phase pipe flow have been calculated on the one hand using a fixed plane distance and on the other hand by applying the calculated plane distance map. The two-phase flow was experimentally generated within a vertical DN50 pipe (inner diameter 54 mm) at superficial liquid velocity of 0.405 m/s and superficial gas velocity of 0.0367 m/s. The time shift $\Delta t(x, y)$ has been determined by cross-correlation of image sequences of 15 s length in order to derive the stationary

velocity field. At first, velocity distributions of the undisturbed and thus axially symmetric bubbly flow have been calculated (Figure 14). Beside the cross-sectional distribution, radial profiles of each quadrant have been determined by averaging over the respective segments. As can be seen, the four profiles of the different quadrants are in better agreement when using the plane distance map compared to a fixed plane distance, which implies that the plane distance map is closer to the truth. The relative deviation of the radial profiles are different for the quadrants in positive or negative y-direction, as can be expected from the plane distance map. At the same time, the overall radial profile of the examined two-phase flow, averaged over the full 360°, differs only in the range of ± 1 % between the two approaches. Thus, it can be concluded that the plane distance map improves the accuracy of determined velocity distributions, but the assumption of a fixed plane distance is still appropriate for axis symmetric flows.
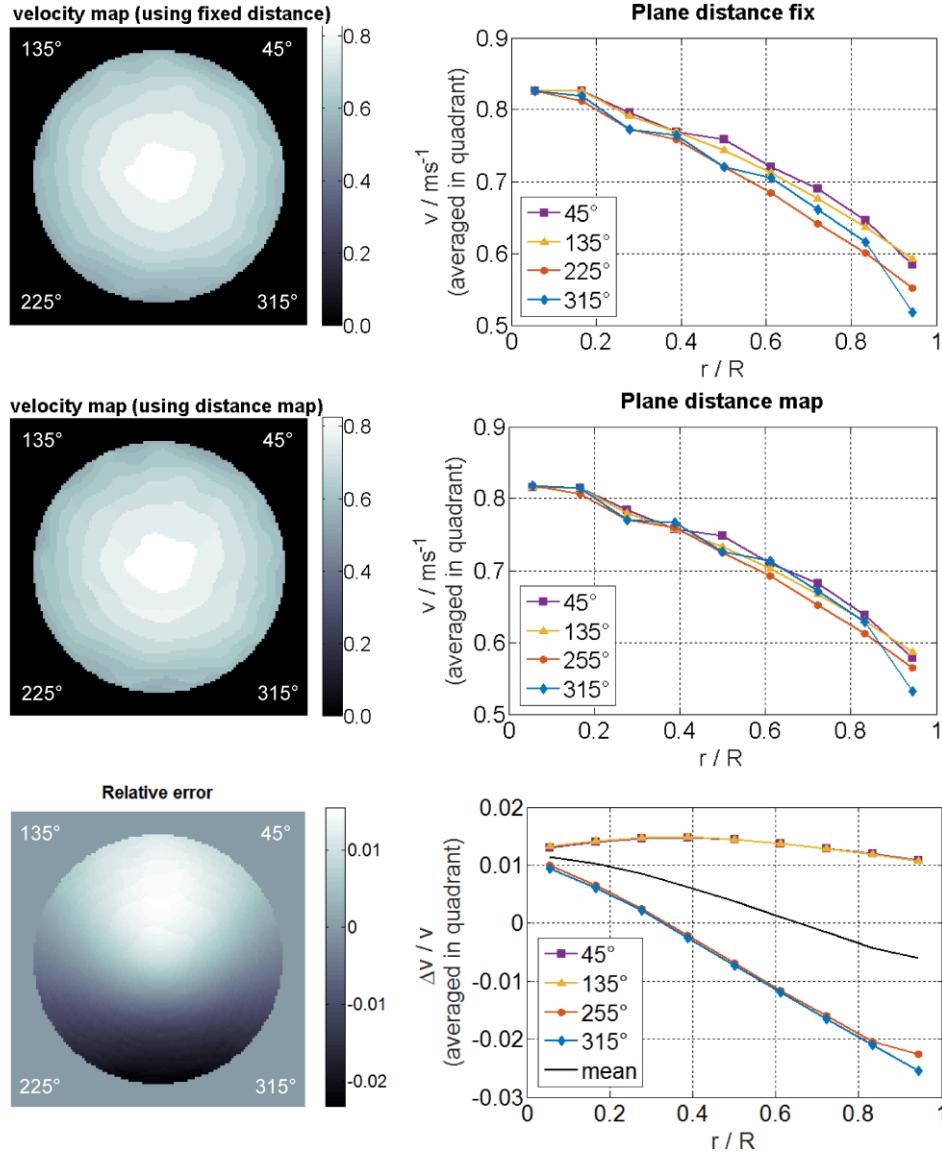
Figure 14: Comparison of velocity maps and radial profiles derived from tomographic data of an axially symmetric two-phase bubbly flow based on a fixed plane distance and a plane distance map.

The importance of distributed velocity information becomes even more apparent in the second considered flow situation, which shows asymmetric flow conditions of the bubbly pipe flow 400 mm behind a half circular obstacle with the same diameter as the pipe (Figure 15). In this case, averaging over larger regions, as is done e.g. for an overall radial profile, is no longer valid and therefore, deviations in the plane distance have a more severe effect on the derived velocities. Nevertheless, the cross-section averaged velocity is only little effected and lies in both flow scenarios well below 1 %.
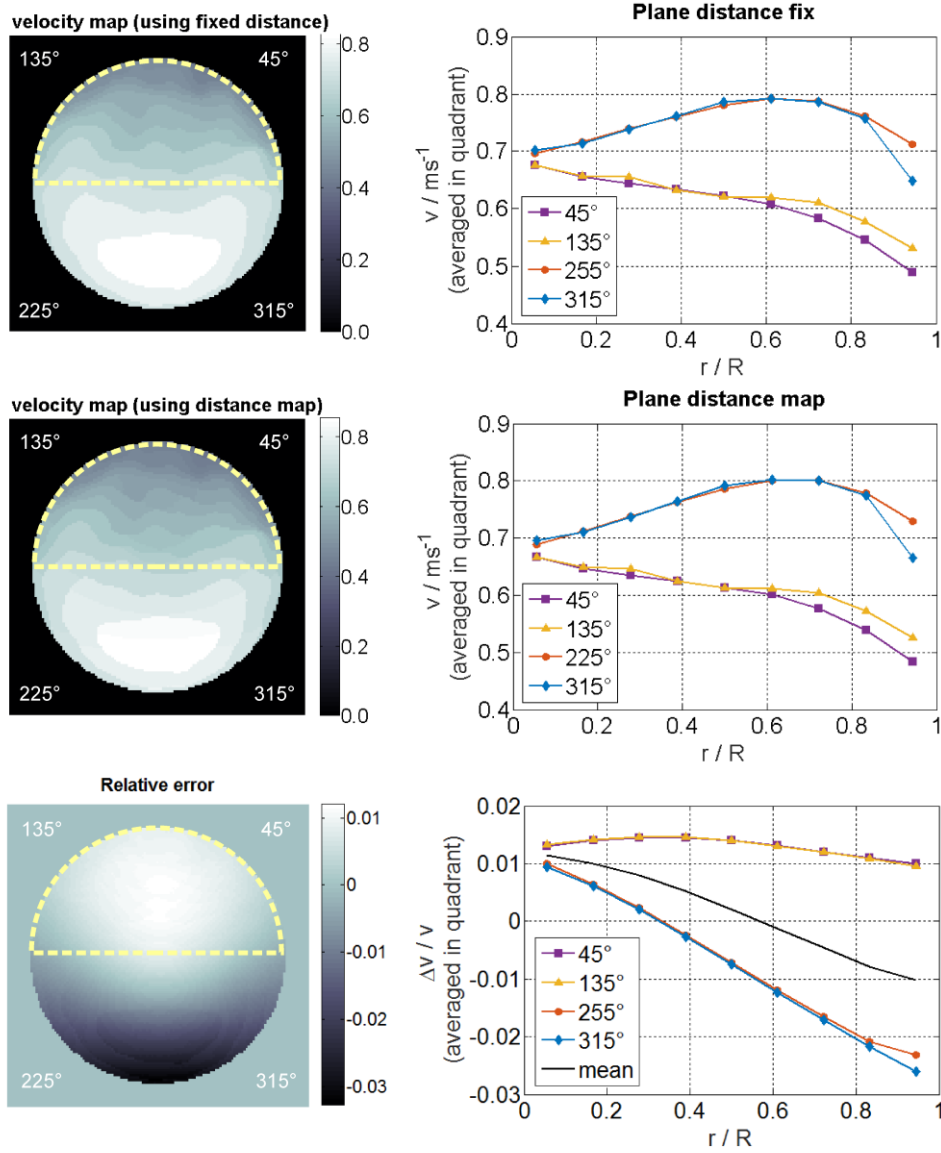
Figure 15: Comparison of velocity maps and radial profiles derived from tomographic data of an asymmetric two-phase bubbly flow 400 mm behind an obstacle (indicated with dashed contour) based on a fixed plane distance and a plane distance map.

Although only one exemplary flow has been analyzed with a single method for the determination of the time-shift between both planes, some general conclusions can be drawn from it. If velocity distributions are of interest, the application of the plane distance map leads to results that are more accurate. For cross-sectional averaged velocities, however, the deviations compared to a fixed plane distance are negligible. In general, the accuracy of the velocity determination depends on the plane distance in a way that larger distances increase the accuracy in the time-shift measurement at a given measurement rate, but impede the correlation of signals as the assumption of constant

velocities between the two sensors does not hold. However, differences within the plane distance distribution are small enough not to have large effects on these general relationships.

4. Conclusions

In this study, the special conditions of dual plane ultrafast electron beam X-ray CT imaging have been analyzed with the aim to improve the accuracy of axial structure velocity measurement via a time-of-flight method. While the accuracy of the time shift measurement is limited by the temporal resolution of the sensor device and the axial velocity to be measured, deviations in the measurement of the sensor distance are normally negligible. However, due to a small axial offset between the focal spot paths of the X-ray source and the detector rings in UFXCT, the calculation of a plane distance is not straight forward. As the regions, from which projection data for 2D tomographic imaging is gathered, are not planar and furthermore asymmetrically shaped, an axial plane distance map is more accurate for velocity derivation than a single axial distance value. Such maps have been derived by a 3D forward projection approach for different parameter combinations of the focal spot paths on the X-ray target. In all cases, the plane distance increases towards the opening of the target. It turned out that the shape of the distance map significantly depends on the focal spot size, whereas the location of the focal spot paths mainly influences the mean plane distance. The latter depends almost linearly on the axial distance of the focal spot paths with a factor of about 0.3.

For validation of the results and evaluation of the focal spot paths parameters, an experimental study has been performed based on a uniformly moving tooth belt at different locations within the cross section of the UFXCT scanner. The time shift between both measurement planes has been derived by cross-correlation of the averaged attenuation value in the image section containing the tooth belt in the tomographic images sequences. The velocity of the tooth belt has been monitored using high precision light barriers so that the measured time shift is directly related to the effective plane distance. The repetitive known structure of the tooth belt allowed a statistical analysis of the time shift and thus the resulting plane distance at the respective position could be determined with a

confidence interval of ±0.05 mm. The comparison between the measurements and calculations showed good agreement concerning the shape of the plane distance map at a reasonable focal spot size. Also the position of the focal spot paths was near to the expected value. Therefore, it was concluded that the map with the best fit to the measurements could be assumed to correlate with the true geometrical focal spot path conditions and the resulting effective plane distance distribution. In order to investigate the effect of using a plane distance map instead of a fixed distance value for velocity determination, both cases have been analyzed using real two-phase flow data sets. As no further gold standard for the velocity distribution was available, only the differences between both cases could be evaluated. A better agreement of the radial profiles of the four quadrants within an axisymmetric flow could be achieved with the plane distance map. It implies that the velocity values derived from the plane distance map are also more accurate in the case of the asymmetric flow, where it is even more important to have spatially resolved results. However, the overall velocity, averaged over the whole cross-section, was little affected by the usage of a plane distance map instead of a fixed distance.

Acknowledgement

REFERENCES

[1]   Fischer F, Hoppe D, Schleicher E, Mattausch G, Flaske H, Bartel R and Hampel U 2008 An ultra fast electron beam x-ray tomography scanner *Meas. Sci. Technol.* **20** (9) 94002

[2]   Fischer F and Hampel U 2010 Ultra fast electron beam X-ray computed tomography for two-phase flow measurement *Nucl. Eng. Des.* **240** (9) 2254–2259

[3]   Banowski M, Beyer M, Szalinski L, Lucas D and Hampel U 2017 Comparative study of ultrafast X-ray tomography and wire-mesh sensors for vertical gas–liquid pipe flows *Flow Meas. Instrum.* **53** 95-106

[4] Rabha S, Schubert M, Grugel F, Banowski M and Hampel U 2015 Visualization and quantitative analysis of dispersive mixing by a helical static mixer in upward co-current gas-liquid flow *Chem. Eng. J.* **262**, 527–540

[5] Zalucky J, Claußnitzer T, Schubert M, Lange R and Hampel U 2017 Pulse flow in solid foam packed reactors: Analysis of morphology and key characteristics *Chem. Eng. J.* **307** 339–352

[6] Verma V, Padding J T, Deen N. G., Kuipers J A M, Bieberle M, Wagner M and Hampel U 2014 Bubble dynamics in a 3-D gas-solid fluidized bed using ultrafast electron beam X-ray tomography and two-fluid model, *AIChE J.*. **60** (5) 1632–1644

[7] Bieberle M and Barthel F 2016 Combined phase distribution and particle velocity measurement in spout fluidized beds by ultrafast X-ray computed tomography *Chem. Eng. J.* **285** 218–227

[8] Kak A and Slaney M 1988 *Principles of Computerized Tomographic Imaging* (New York: IEEE Press)

[9] Barthel F, Bieberle M, Hoppe D, Banowski M and Hampel U 2015 Velocity measurement for two-phase flows based on ultrafast X-ray tomography *Flow Meas. Instrum.* **46** 196–203

[10] Buzug T 2004 *Einführung in die Computertomographie. Mathematisch-physikalische Grundlagen der Bildrekonstruktion* (Berlin, Heidelberg: Springer-Verlag)

[11] Barthel F 2016 *Ultraschnelle Röntgencomputertomographie für die Untersuchung von Zweiphasenströmungen* (Dresden: TUDpress, w.e.b. Universitätsverlag & Buchhandel)